Spatial frequency domain imaging for the longitudinal monitoring of vascularization during mouse femoral graft healing

JINGXUAN REN,[1,*] GABRIEL A. RAMIREZ,[2] ASHLEY R. PROCTOR,[1] TONG TONG WU,[3] DANIELLE S. W. BENOIT,[1,2,4,5,6] AND REGINE CHOE[1,7]

[1]*Department of Biomedical Engineering, University of Rochester, Rochester, NY 14627, USA*

[2]*Department of Orthopaedics and Center for Musculoskeletal Research, University of Rochester, Rochester, NY 14642, USA*

[3]*Department of Biostatistics and Computational Biology, University of Rochester, Rochester, NY 14642, USA*

[4]*Department of Chemical Engineering, University of Rochester, Rochester, NY 14627, USA*

[5]*Department of Biomedical Genetics and Center for Oral Biology, University of Rochester, Rochester, NY 14642, USA*

[6]*Materials Science Program, University of Rochester, Rochester, NY 14627, USA*

[7]*Department of Electrical and Computer Engineering, University of Rochester, Rochester, NY 14627, USA*

*Jingxuan.Ren@rochester.edu

Abstract: Allograft is the current gold standard for treating critical-sized bone defects. However, allograft healing is usually compromised partially due to poor host-mediated vascularization. In the efforts towards developing new methods to enhance allograft healing, a non-terminal technique for monitoring the vascularization is needed in pre-clinical mouse models. In this study, we developed a non-invasive instrument based on spatial frequency domain imaging (SFDI) for longitudinal monitoring of the mouse femoral graft healing. SFDI technique provided total hemoglobin concentration (THC) and oxygen saturation (StO$_2$) of the graft and the surrounding soft tissues. SFDI measurements were performed from 1 day before to 44 days after graft transplantation. Autograft, another type of bone graft with higher vascularization potential was also measured as a comparison to allograft. For both grafts, the overall temporal changes of the measured THC agreed with the physiological expectations of vascularization timeline during bone healing. A significantly greater increase in THC was observed in the autograft group compared to the allograft group, which agreed with the expectation that allografts have more compromised vascularization.

1. Introduction

Bone grafting is the common treatment for critical-sized bone defects, which cannot heal without intervention. Each year, more than 500,000 bone graft procedures are performed in the United States and more than 2.2 million worldwide [1,2]. Among common types of bone grafts, autograft utilizes healthy bone and soft tissues from the non-load bearing regions of the same patient. Autograft usually achieves complete healing but is limited by the tissue availability and donor site morbidity [1–3]. Currently, allograft, which utilizes the bone from cadavers, is the clinical gold standard of treating critical-sized bone defects. Allograft is heavily devitalized to inhibit immunogenicity. However, the devitalization process removes osteogenic tissues in the graft such as periosteum, which is critical in bone injury healing. As a result, bone healing is compromised in allograft and a 60% long-term failure rate was observed [4,5]. To improve allograft healing, new treatment methods are being developed based on preclinical mouse femoral graft models [6–11]. For example, a hydrogel-based tissue-engineered periosteum is under development to

transplant mesenchymal stem cells (MSCs) onto allograft surface [6,7]. This method is believed to enhance graft vascularization, bone formation and biomechanical strength, which are typically observed for bone healing assessment.

Among these aspects of bone healing, vascularization, i.e., the development of blood vessels, is regarded as a critical process, since vasculature development is a precursor of the bone formation [12–14]. Blood vessels deliver nutrients, oxygen, growth factors and circulating cells to the injury sites [12–16]. Here, we focus on the blood volume in the vasculatures in the bone graft and the surrounding tissues. Traditional method of measuring blood volume in preclinical mouse models is based on radiographic techniques [6–9,17,18]. Briefly, lead-based contrast agent is perfused throughout the animal and cured in the blood vessels. The hindlimb is then harvested and immersed in acid to demineralize the bone. The blood vessels in the bone can be exposed by demineralization and imaged by micro-computed tomography (micro-CT). The typical spatial resolution of micro-CT is high enough to image the vasculatures of ~10 μm. However, the method is terminal, thus no longitudinal observation is possible. Magnetic resonance imaging (MRI) is a potential method for longitudinal assessment of the vasculatures [19], but its high cost makes it unsuitable for frequent monitoring. Photoacoustic tomography (PAT) can potentially provide *in vivo* longitudinal vascularization monitoring [20]. However, since PAT is based on ultrasound detection, the acoustic barrier effect of the bone makes it difficult to measure the vasculatures within the bone [21].

In this study, we employed spatial frequency domain imaging (SFDI) as an inexpensive, non-invasive method for longitudinal monitoring of the vascularization during mouse femoral graft healing. SFDI is a wide-field diffuse optical technique for extracting absorption and reduced scattering coefficients of turbid media [22,23]. With multiple wavelengths, SFDI can provide concentrations of oxy- and deoxy-hemoglobins of the biological tissue. SFDI has been widely applied in both animal (e.g., mouse brain/tumor, pig/rat skin flap/burn model) and human (e.g., skin lesions, skin flap, *ex vivo* tumors) studies [24–31]. In the mouse femoral graft model, higher total hemoglobin concentration (THC) is expected in autografts than in allografts, as autografts are usually better vascularized, and more blood contents exist in a unit volume of tissue [6,7]. In the following section 2, we first present our in-house SFDI instrument and the tissue phantom validation method. Then the details of the longitudinal experiment on mice with autograft and allograft is described. In section 3, the results from the tissue phantom experiments and *in vivo* monitoring are presented. Finally, the significance of the study, physiological observations and limitation are discussed in section 4.

2. Material and methods

2.1. SFDI instrumentation

An in-house SFDI instrument was built for the *in vivo* measurements of the mouse hindlimb. The schematic and the photo of the setup are shown in Fig. 1. Two light-emitting diodes (LED660L and LED851L, Thorlabs, Newton, NJ) with central wavelengths of 660 nm and 850 nm were used as light sources. The illumination patterns were generated by a digital micromirror device (LC4500, Keynote Photonics, Allen, TX). A complementary metal-oxide semiconductor (CMOS) camera (DCC3240N, Thorlabs, Newton, NJ) was employed to collect the diffuse reflected light from the sample.

The SFDI technique used in this study was introduced by Cuccia *et al.* [22,23]. Briefly, sinusoidally modulated illumination was projected to the sample. Six spatial frequencies, ranging from 0 to 0.05 mm^{-1} with a step size of 0.01 mm^{-1}, were used to generate the illumination patterns. For each spatial frequency, three phase-shifted images with 120° separation were generated sequentially for the extraction of the AC component of the diffuse reflectance R_{AC}. By normalizing R_{AC} to the reference measurement performed on tissue phantoms with known optical properties, we fit the data with the diffusion theory model based on homogeneous, semi-infinite
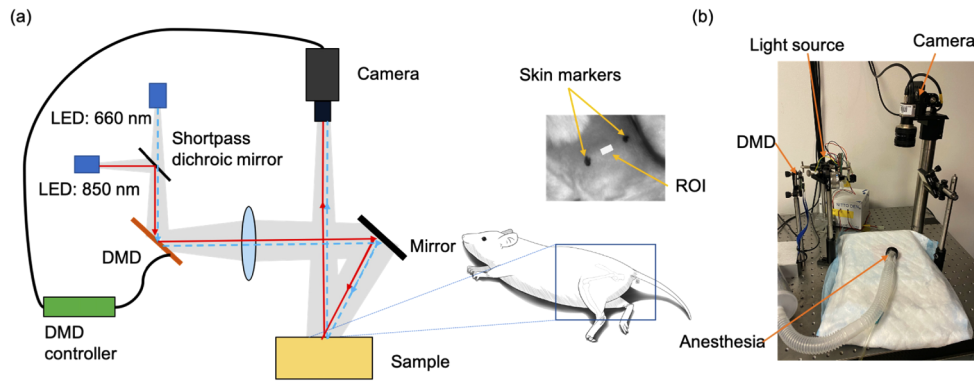
Fig. 1. (a) Schematic of the SFDI instrumentation and the positioning of the mouse in the *in vivo* measurement. The inlet photo shows the skin markers and the region of interest (ROI) indicating the graft position. LED: light-emitting diodes; DMD: digital micromirror device. (b) A photo of the setup. Light source includes the LEDs and the shortpass dichroic mirror.

medium [22,23] to obtain the absorption (μ_a) and reduced scattering (μ_s') coefficients of the sample. Such process was applied for both wavelengths to derive the concentrations of the oxy- (HbO_2) and deoxy-hemoglobin (Hb) for *in vivo* experiments (to be described later).

2.2. Accuracy of the SFDI technique in quantifying optical properties of tissue phantoms

Tissue phantom experiments were performed to validate our SFDI technique in quantification of the optical properties of turbid media. Since the lateral side of the mouse hindlimb is fairly flat, homogeneous liquid phantoms were used as a simplified geometry to test the accuracy of SFDI in quantifying optical properties. Tissue phantoms with multiple absorption coefficients were measured for both wavelengths. The phantoms were made by mixing the distilled water, nigrosin ink and Intralipid (Fresenius Kabi, Uppsala, Sweden). The absorption coefficients of the nigrosin ink was calibrated by a spectrophotometer (Cary 60 UV-Vis, Agilent, Santa Clara, CA) as the gold standard. The absorption coefficients were adjusted from a low value (0.03 mm^{-1} for 660 nm, 0.01 mm^{-1} for 850 nm) to a high value (0.08 mm^{-1} for 660 nm, 0.04 mm^{-1} for 850 nm) to mimic the widely changing hemoglobin concentration of the *in vivo* tissue during the graft healing. The reduced scattering coefficient was kept constant as 1.8 mm^{-1} (660 nm) and 1.2 mm^{-1} (850 nm), which is typical for the tissues of the mouse hindlimb from our *in vivo* measurement.

2.3. Overview of the in vivo vascularization monitoring experiment

Two groups of mice with different types of femoral graft transplantation were monitored by SFDI from one day prior to the graft surgery to day 44 post-surgery. One group (n=5) was transplanted with autografts and the other (n=5) with allografts.

The SFDI measurements were performed on a daily basis during the first two weeks. After two weeks of daily monitoring, the mice started to develop resistance to the anesthesia. This led to increased level and prolonged duration of anesthesia for imaging preparation, which could potentially result in animal death if continued. Therefore, the measurement frequency was reduced to twice a week in the following weeks. The timeline of the experiment is shown in Fig. 2. During the first 6 days post-surgery, the skin covering the graft site was covered by black nylon sutures, which contaminated the SFDI signal. From day 7 post-surgery, the skin wound healed and the nylon sutures from all the mice were taken off. Therefore, the data from day 1 to
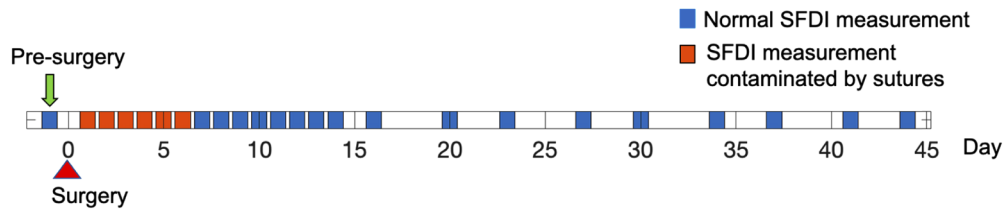
Fig. 2. Timeline of the longitudinal monitoring. For each mouse, the SFDI measurement started from one day before the graft surgery and stopped at day 44 post-surgery. The measurement frequency decreased after week 2 due to the resistance to anesthesia. The data in the first week was contaminated by black sutures covering the wound site and was not included in the analysis.

6 post-surgery was not used in the analysis. All experimental protocols were approved by the University Committee on Animal Resources (UCAR) at the University of Rochester.

2.4. Preclinical femoral graft model

In this study, 10 female 6-week-old BALB/cByJ mice (Jackson Laboratory, Bar Harbor, Maine) were measured. For both groups, the graft was surgically introduced to the left femur of each mouse. First, an incision was made in the skin on the lateral side of the hindlimb. The femur was exposed by reflecting the skin and skeletal muscle using blunt dissection. Then a rotary tool (Dremel, Mount Prospect, IL) with two parallel diamond wheels attached was used to cut the mid-diaphysis of the femur. The distance between the two wheels were fixed to control the length of the bone defect as 4 mm. Such distance is ensured to create a critical-sized bone defect in the mouse femoral model [6,7,9]. The graft was stabilized to the host bones by a 26G intramedullary pin, which was inserted through the medullary cavity and bent at the proximal and distal ends of the femur. The skeletal muscle and skin were closed with nylon sutures, which were removed at day 6 post-surgery. Sustained release buprenorphine was administered perioperatively per UCAR policy on rodent analgesia. For the autograft group, the autograft was the same bone segment cut from the femur. The autograft was flipped to create some mismatch at the conjunction to the host bones. For the allograft group, the allograft was harvested from femurs of C57BL/6 mice (age-matched with the BALB/cByJ mice). The harvested allografts were heavily processed to remove the soft tissues and devitalized in -80°C environment before implantation.

2.5. In vivo SFDI measurements

During the measurement, the mouse was first anesthetized by isoflurane. The mouse was placed laterally with the left hindlimb exposed to the illumination. The hair covering the hindlimb was removed before imaging. The region of interest (ROI) was identified with skin markers. Two skin markers were made at the ends of the femur via palpation before imaging to indicate the location of the femur. A 4 mm × 2 mm square ROI was generated in the middle of the two skin markers (Fig. 1(a) inset). To do so, centers of the skin markers were identified manually and connected by a line segment. The square ROI was generated so that its centroid was at the midpoint of the line segment and its long axis aligned with the line segment. Since the bone graft is located at the mid-diaphysis and has a length of 4 mm, such ROI approximately covers the graft region.

For further analysis, the mean and standard deviation of THC and StO_2 within the ROI were extracted from each mouse at each day. To account for the variation among individuals, relative mean THC and StO_2 were defined as the average THC and StO_2 normalized by the corresponding average values of the mouse at pre-surgery for visualization (to be shown in figures in Results section).

2.6. Repeatability of the in vivo measurements

Daily *in vivo* measurements were performed on 5 healthy mice for 9 days to estimate the *in vivo* temporal stability of our SFDI technique. The mice were at the same age (6-week-old) as those in the graft monitoring experiment when the first measurement started. The measurement protocol was the same as described in section 2.5.

2.7. Statistical analysis for the longitudinal monitoring

SAS version 9.4 (SAS Institute Inc., Cary, NC) was used for the statistical analyses. To account for the repeated measurements within each individual mouse, a linear mixed-effect (LME) model was employed to analyze the average absolute THC within the ROI in the longitudinal study. The model is described as follows:

$$THC = \beta_0 + \boldsymbol{\beta_1} t + \beta_2 g + \boldsymbol{\beta_3} t * g + \mathbf{Z}\boldsymbol{\gamma} + \varepsilon, \tag{1}$$

where t is the time (day) set as a categorical variable with 18 levels (i.e., 18 time points), g is the graft type (0 for allograft and 1 for autograft), $\mathbf{Z}$ is the design matrix of random effects (mouse ID), $\boldsymbol{\gamma}$ is the vector of random-effects and ε is the random error. The intercept β_0 indicates the overall mean of THC, $\boldsymbol{\beta_1}$ is the regression coefficients vector of t to indicate the change in THC from baseline, and β_2 is the regression coefficients of g. The fixed-effect coefficient vector $\boldsymbol{\beta_3}$ of the interaction term $t * g$ indicates the difference in THC change from baseline between the two graft types. By setting t as a categorical variable, this LME model does not require a linear relationship between t and THC. The intra-subject correlation (i.e., repeated measures for each mouse) was captured by the Toeplitz covariance matrix with two bands [32].

3. Results

3.1. Tissue phantom experiments

The optical properties of the tissue phantoms recovered by our SFDI system was shown in Fig. 3. For both wavelengths employed in this study, our SFDI system recovered the μ_a with <6% discrepancy from the ideal values derived from spectrophotometry. Although the μ_s' recovered by the SFDI has a tendency to change when the μ_a was higher, the discrepancy from the ideal value was within 4%. The results show the capability of our SFDI technique in quantifying the optical properties of tissue phantoms.

3.2. Repeatability of the in vivo measurements

The relative THC and StO_2 from the repeated *in vivo* measurement were shown in Fig. 4. The daily measurement for 9 days indicated the fluctuation of the hemodynamic parameters in the healthy mice. In general, the temporal change of THC was within 20%, and the change of StO_2 was slightly higher but still within 30% for individual mouse. The fluctuation of the group-averaged relative THC and StO_2 were both under 12%.

3.3. Longitudinal SFDI measurements of mouse femoral grafts

Examples of the SFDI-derived images of THC and StO_2 are shown in Fig. 5. The photos indicating the ROI with respect to the skin markers are also included. The skin in the ROI was fairly flat. The skin markers and the peripheral regions beyond the thigh appeared to show unusually high THC values (>200 μM). These high THC regions did not affect the subsequent analyses as they were not part of ROI. Qualitatively, the autograft mouse appeared to have higher THC than the allograft mouse in the ROI. The extracted relative mean THC and StO_2 acquired from the longitudinal SFDI measurements for each mouse are presented in Fig. 6(a,b). The error
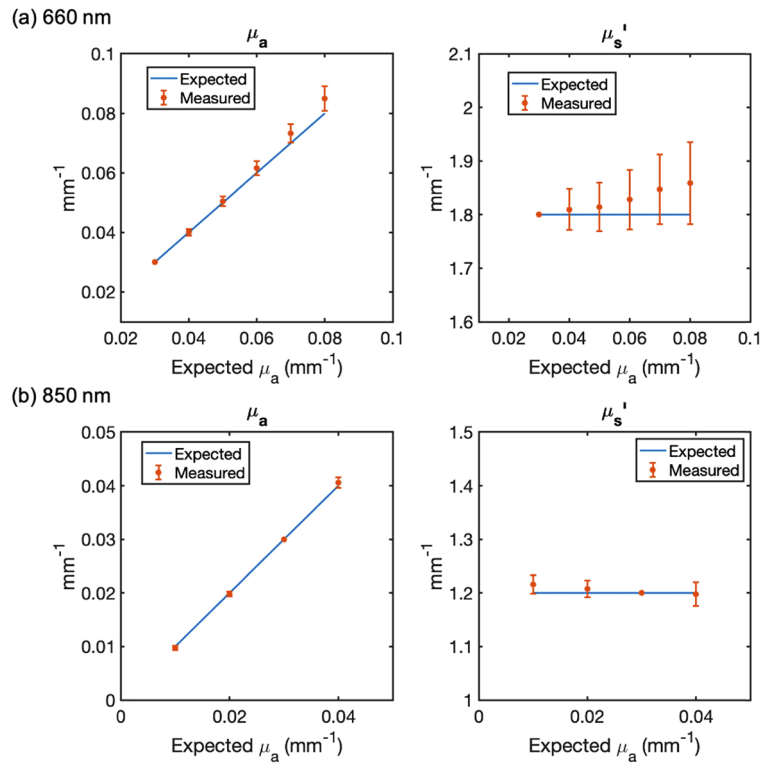
Fig. 3. Recovered optical properties of the tissue phantoms. The measured average μ_a and μ_s' are plotted against the expected values for (a) 660 nm and (b) 850 nm illuminations. The error bar indicates the standard deviation among pixels. In all cases, the discrepancy between the measured and expected values were below 6%.

bar indicates the standard deviation within the ROI defined in section 2.5 normalized by the pre-surgical (healthy) level of each individual mouse.

An elevation of the THC was observed for all the mice at day 7 post-surgery, when the uncontaminated data were available. During the second week of the healing, THC from both groups showed a gradual declining trend. After day 14, the autograft mice appeared to have higher relative THC, while the allograft mice appeared to remain in a relative low level of relative THC. However, such difference of trends between the groups were not observed in StO_2, where the two groups overlapped with each other for most of the days. Figure 6(c,d) shows the group average of the relative THC and StO_2, respectively. The error bar indicates the standard error of mean for each graft type. The relative THC of the autograft group appeared to be above 1.3 while those of the allograft remained around 1.2 after day 14.

3.4. Statistical analysis

The type III analysis [32] of the LME model shows a statistical significance of time t and its interaction with graft type g (both p<0.001) (Table 1). The fixed-effect coefficient vector $\boldsymbol{\beta_1}$ associated with t are the change of THC against baseline. The low p-value suggests a significant change of THC over time t for both graft types. The fixed-effect coefficient vector $\boldsymbol{\beta_3}$ of the interaction term $t * g$ indicate the differences in change of THC compared to baseline between the two graft types. The model showed that autograft group has a significantly greater increase in THC compared to the allograft.
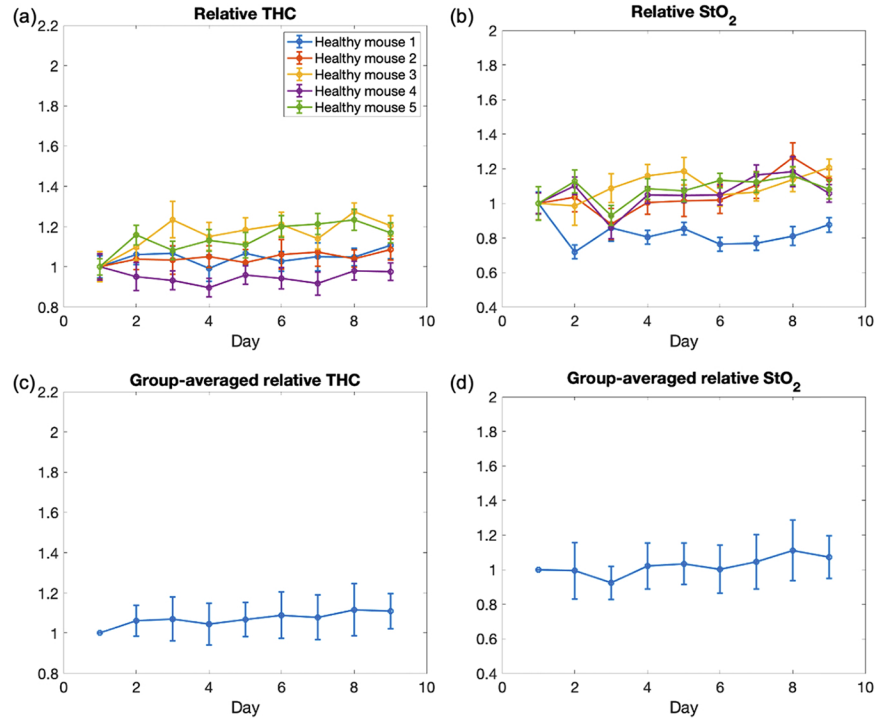
Fig. 4. Relative THC and StO_2 of the healthy mice (n=5) during 9 days of monitoring. (a, b) Relative mean THC and StO_2 within the ROI (defined in section 2.5) for each healthy mouse. The error bar indicates the standard deviation of the quantity (THC or StO_2) normalized by the pre-surgery mean of the corresponding mouse. (c, d) Group-averaged relative THC and StO_2. The error bar indicates the standard error of the group mean.
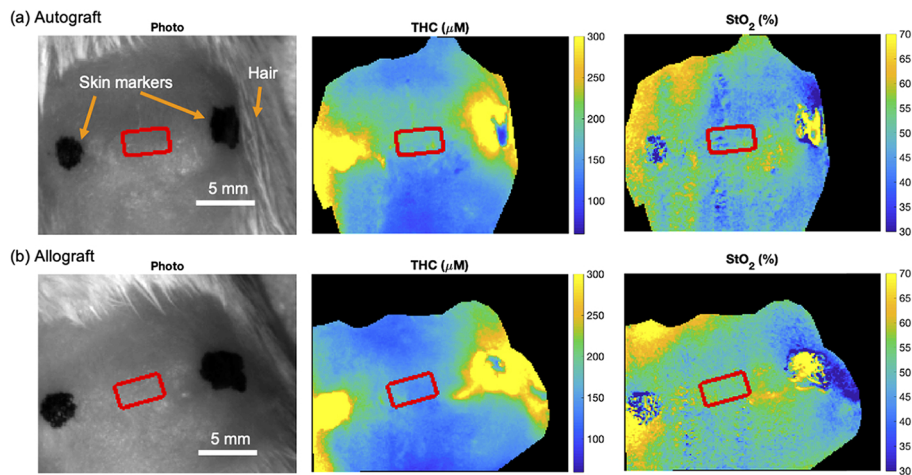

Fig. 5. Examples of the photo, THC and StO_2 images. (a) and (b) show the images of an autograft and an allograft mouse, respectively. In THC and StO_2 images, the hair regions are shown in black. The red box indicates the ROI defined in section 2.5, where the graft is approximately located. The femur was between the two skin markers (left: distal, right: proximal) and the skin covering the femur was relatively flat.
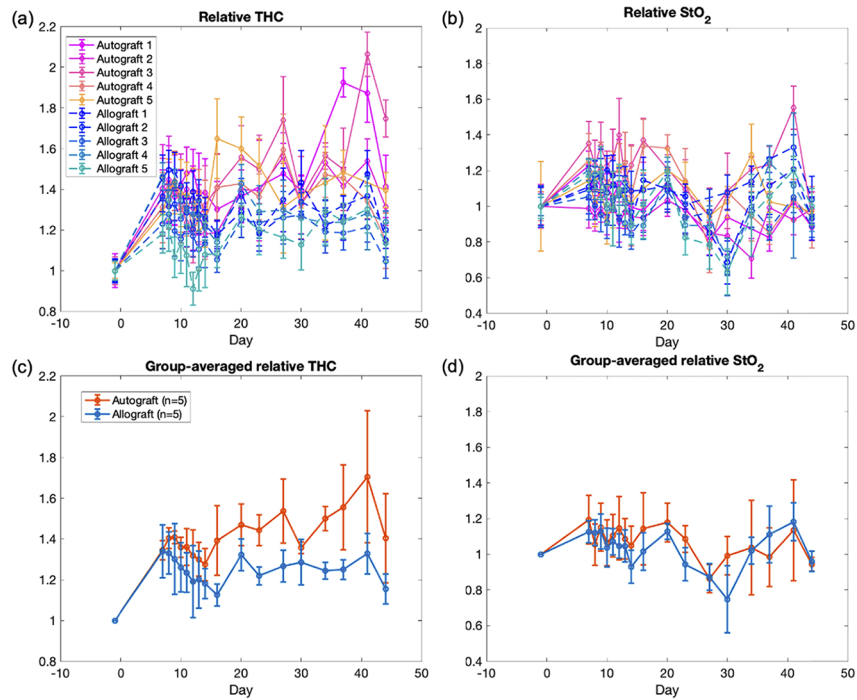
Fig. 6. Relative THC and StO_2 of the graft mice from longitudinal monitoring. (a, b) Relative mean THC and StO_2 within the ROI for each mouse. The error bar indicates the standard deviation of the quantify (THC or StO_2) normalized by the pre-surgery average of the corresponding mouse. (c, d) The group-averaged relative THC and StO_2 for each graft type. The error bar indicates the standard error of the group mean. For THC, the autograft group showed significantly greater change compared to the allograft group.

Table 1. Result of the linear mixed-effect fitting[a]

			Type III Tests of Fixed Effects			
Effect	Num DF	Den DF	Chi-Square	F Value	Pr > ChiSq	Pr > F
Group (g)	1	132	2.33	2.33	0.1272	0.1296
Time (t)	17	132	183.05	10.77	<.0001	<.0001
Group*Time ($t * g$)	17	132	44.94	2.64	0.0002	0.0010

[a]Type III tests are the hypothesis tests for each of the variables in the LME model individually. Num DF: numerator degrees of freedom (in the F test); Den DF: denominator degrees of freedom (in the F test); Chi-Square: Chi-Square statistics; F Value: F statistics; Pr: probability.

4. Discussion

4.1. Significance of the study

This is the first demonstration of the SFDI technique applied in a mouse bone healing study. The SFDI technique provides a non-contact, non-invasive and inexpensive method to longitudinally monitor the THC and StO_2 during mouse bone healing. We developed a protocol for the mouse femoral graft model measurement. The practical frequency of measurement for monitoring mouse femur healing was investigated. For both graft types, significant changes of THC over time were observed, suggesting changes in vasculature due to healing. For the two bone graft types, we observed significant difference in the change of THC during healing. The observation agrees with the expectation that autograft has better vascularization than allograft. The results show the potential of SFDI as a functional imaging technique suitable for frequent *in vivo* measurement in pre-clinical studies.

Traditional methods of vasculature evaluation are often terminal, such as contrast agent-mediated micro-CT and immunohistochemistry. These methods require animal sacrifice therefore the longitudinal monitoring is impossible. The usual practice is to use more animals and sacrifice a subset of them to acquire data at a certain time point. *In vivo* methods for vasculature evaluation include magnetic resonance imaging (MRI), positron emission tomography (PET) and single photon emission computed tomography (SPECT) [19]. However, they are costly and not suitable for frequent longitudinal monitoring. Due to the lack of frequent monitoring technique, researchers usually provide data at limited time points in the orthopedic research community. This practice may miss important physiological processes during bone healing/development. For example, to monitor the graft healing process spanning 9 weeks, having measurements every 3 weeks using terminal methods was adequate to observe vascularization difference among various grafts [7]. However, the soft callus formation usually occurs in 5-10 days post-injury, while hard callus formation occurs in 16-21 days post-injury [13]. Such low frequency (i.e., every 3 weeks) can easily miss these important stages, while increasing the measurement frequency will significantly increase the cost and animal sacrifice.

Our SFDI technique paves an economic way for frequent longitudinal monitoring. As demonstrated in this study, our SFDI technique shows the capability of daily monitoring. The measurement frequency was currently limited by the animal tolerance to anesthesia, not by the SFDI technique. Other non-invasive techniques are not suitable to provide such frequent monitoring of vascularization either due to high cost or incompatibility with bone. The ability to monitor frequently is critical when the hemodynamic changes are rapid (e.g., inflammation, soft callus formation). Frequent monitoring also unveils the unknown hemodynamic trend so that the optimal measurement frequency can be adjusted accordingly for future studies. Based on our observation, two measurements per week may be sufficient after day 7 post-surgery since the daily measurement during week 2 showed almost monotonically varying THC and uniform StO_2.

4.2. Physiological observations

Our observations indicate that hemodynamic changes during graft healing measured by SFDI are in agreement with expected physiological changes in mouse femoral closed fracture [13,15,33,34]. To illustrate this point, the timeline from literatures are briefly summarized in the following paragraphs. The graft healing usually shares a similar process to the fracture healing with a delayed timeline due to the larger defect size than a simple fracture [6–8]. However, the exact timeline is unclear in literatures probably due to the lack of longitudinal quantification method.

At the beginning of the mouse femoral fracture, the vasculatures in and around the bone are disrupted and the blood accumulates to form hematoma around the bone defect site [33,34]. The inflammation is initiated and vasodilation occurs in the surrounding tissues (day 0-5) [15]. Both factors cause increased blood volume in the tissues surrounding the bone defect site. The

hematoma then develops into fibrinous thrombus (i.e., clot). The capillaries start to grow into the clot to clear debris. The second stage of the bone healing is endochondral bone formation (day 5-16). The soft callus forms to be the basis of the bony callus and provide the mechanical support. While angiogenesis remains and the vessels deliver the cytokines, growth factors, nutrients and circulating cells to the defect site, the soft callus is principally avascular (i.e., lack of vasculatures) [33]. During this stage, the blood volume is expected to be lower in soft callus compared to that of the hematoma. The gradual decrease of THC during week 2 observed in our SFDI measurements may be due to this process (Fig. 6).

The soft callus is then mineralized to hard callus in the third stage of healing (day 16-21). Such process requires extensive support from vasculatures for osteoblasts to differentiate. In the last stage of bone healing, osteoclasts resorb the hard callus and osteoblasts form the new bone (day 21-35). Together the mineralized matrix tends to be remodeled to its pre-injury structure. The vascularization process is maintained in this stage [13,33]. From our SFDI monitoring, the mildly growing THC after day 14 matches the development of vasculatures during the hard callus formation and remodeling stages. For most of the days, the relative THC of autografts remained at a high level (>1.3), while that of allografts was around 1.2. The values being greater than 1 reflected the maintained neo-vascularization in the healing process causing a higher vascular density than the pre-injury state.

Vascularization is regarded to be more compromised in allograft than in autograft due to the loss of periosteum. Micro-CT angiography has shown more developed vasculatures in autografts than in allografts after week 3 post-injury [6–8,11,17]. The relative THC from our longitudinal monitoring matches such physiological expectation. The autograft mice appeared to have higher relative THC than the allograft mice (Fig. 6). Our LME model suggested that the autograft group had a significantly greater increase of the THC from baseline, compared to the allograft group. Again, this observation agrees with the expectation that allografts have more compromised vascularization.

Oxygenation also has an important role in bone injury healing as it is involved in many processes and affects the activity of skeletogenic cells. Environmental hyperoxia was found to promote vascularization and bone formation [35]. As for the local oxygen level around the bone injury site, there are some ongoing studies but the detailed trend of the oxygenation during bone healing is not fully understood [36].

4.3. Advantage of SFDI for murine hindlimb monitoring, limitations and future directions

As a widefield technique, SFDI is scanning free, therefore the acquisition time can be greatly reduced compared to traditional diffuse optical tomography (DOT) with point sources and detectors. Our current measurement protocol (2 wavelengths, 6 spatial frequencies, including DC) takes ~2 min for each mouse. The speed was limited by the camera exposure time for sufficient signal to noise ratio and could be faster if light sources with higher power were employed. The fast acquisition enables near-simultaneous multi-model imaging and high throughput experiment. It also reduces duration of anesthesia for animals. The pixel-based extraction of optical properties based on analytic solution of a semi-infinite homogeneous geometry is simple while providing two-dimensional spatial information. Such extraction is easy and avoids the tomographic computation. With the simplicity and ease of use, we found significantly different vascularization between two groups with different bone grafts.

These findings, however, need to be interpreted with care, especially in terms of the origin of signals for SFDI. Considering that the center depth of the mouse femur in this study is ~2 mm and the upper surface depth is ~1 mm, we selected lower spatial frequencies from 0 to 0.05 mm^{-1} with a step size of 0.01 mm^{-1} than those generally used by others for deeper penetration [23,24]. According to a Monte Carlo simulation study [37], the median sampling depth of 0.05 mm^{-1} spatial frequency is ~1.2 mm for tissues with $\mu_s'/\mu_a \approx 35$. The sampling depth increases to

~1.5 mm for 0 spatial frequency. It should be noted that the penetration depth changes when the optical properties of the tissue change during the healing process. The μ_a and μ_s' of the hindlimb tissue varied over time during our longitudinal study. For 660 nm, μ_a changed between 0.045 mm^{-1} and 0.075 mm^{-1}, while μ_s' fluctuated around 1.8 mm^{-1}. For 850 nm, μ_a changed between 0.025 mm^{-1} and 0.035 mm^{-1}, while μ_s' fluctuated around 1.2 mm^{-1}. The ratio of $\mu_s'/\mu a$ was mostly between 30 and 40. According to the Monte Carlo simulation study [37], these variations in optical properties result in the median sampling depth between 1.1 mm and 1.6 mm for our spatial frequencies. These depths still reach the upper-center part of the mouse femoral graft. However, the signals are still mixed with those from superficial tissues, and are prone to partial volume effects. For example, Cuccia *et al.* measured the edge response function with two gelatin phantoms assembled side-by-side. When the sample was covered by an extra 2-mm-thick phantom (μ_a=0.01 mm^{-1}, μ_s'=0.5 mm^{-1}), the detected absorption contrast degraded to ~15% of that at the surface [23].

Another source of inaccuracy of the measured absorption and reduced scattering coefficients could be the limited size of the sample. The SFDI theory is based on the semi-infinite and homogeneous medium assumption. However, the size of the mouse hindlimb is usually around 20 mm x 20 mm. The low spatial frequencies of our illumination correspond to spatial periods greater than or equal to 20 mm. Although the ROI was usually in the middle of the hindlimb, we expect discrepancies between the measured reflectance and the SFDI model, leading to reduced accuracy in recovery of absorption and scattering properties.

Despite the several factors affecting the accurate extraction of bone properties, a region of higher μ_s' is observed along the femur region identified by the skin markers on the proximal and distal ends of the femur. Example images of μ_a and μ_s' of a sample mouse from pre-surgery measurement are shown in Fig. 7. The higher μ_s' in femur region agrees with the expectation that the bone has higher μ_s' than muscles [38]. However, the images of μ_a and μ_s' in post-surgical measurements did not show evident shapes of the femur (not shown), which in turn affected the unclear boundary between the ROI and the surrounding regions in the THC and StO$_2$ images (Fig. 5). Despite such unclear boundary, the THC and StO$_2$ within the ROI still provided the physiological information of the mid-diaphysis as the skin markers were made via palpation, which is determined independently of the images.

In order to improve the quantification, we will perform a more extensive analysis of the sensitivity for the illumination pattern selection and optimize a tomographic method for our application. Instead of the semi-infinite, homogeneous medium assumption, a model with animal-specific hindlimb geometry derived from other imaging modality such as *in vivo* micro-CT will be employed to mitigate the partial volume effects. Despite the fact that the SFDI method used in this study does not separate the changes due to the bone and surrounding tissues, we can still see the THC response difference between the two graft types. Perhaps, our measurements were partially reflecting THC responses induced by surrounding soft tissues as they are intensively involved in the healing process, especially the vascularization [13,33]. To investigate the origin of the signals, we will compare the measured THC with the vasculature density acquired from traditional methods such as contrast agent-mediated micro-CT.

The current SFDI technique and the measurement protocol can also be improved in several other aspects. The current setup has only two wavelengths (i.e., 660 nm and 850 nm), which could limit the accuracy of the hemoglobin quantification. With more wavelengths, the SFDI technique could improve the accuracy of hemoglobin concentration quantification. Another potential source of error is the impact of sample curvature. Zhao *et al.* [39] showed that highly curved surface (mouse tumor) can cause severe artifacts in SFDI measurement. In our study, the lateral side of the mouse hindlimb is relatively flat and our repeatability measurement showed good stability of THC in 9 days in this region. However, image artifacts were noted at the periphery of the thigh where curvature was significant. Therefore, applying curvature correction
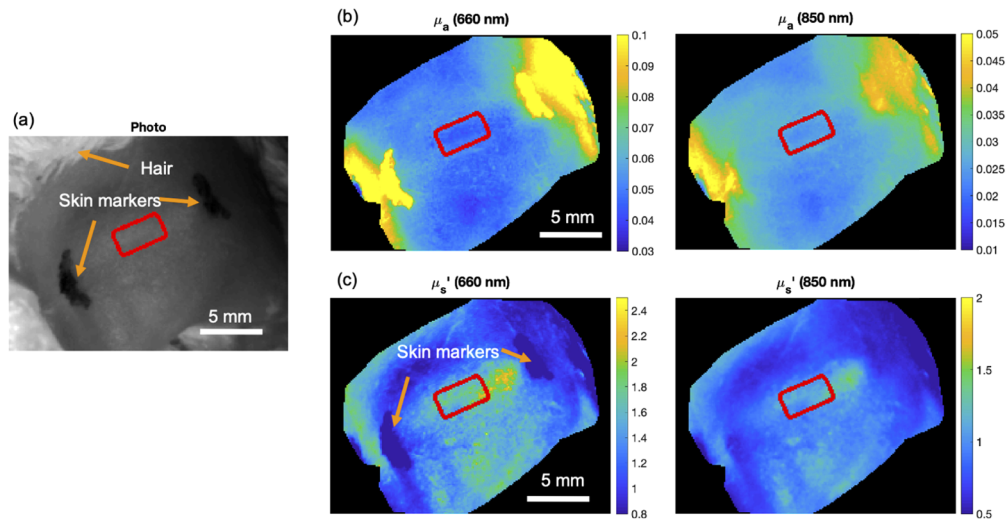
Fig. 7. (a) μ_a and (b) μ_s' images of a representative mouse from pre-surgery measurement. Images of μ_s' from both wavelengths show higher μ_s' in the femur region, which was identified by the skin markers in the proximal and distal ends of the femur. The ROI (red box) defined in the middle of the skin markers covers the mid-diaphysis region. The femur region was not evident in the μ_a images.

could further improve the credibility of the measurement in the future. To avoid the signal contamination during week 1 and investigate early blood volume changes, the black nylon suture could be replaced by transparent sutures or skin glues.

This study is our first step towards the comprehensive hemodynamic monitoring. In the future, our SFDI technique can be combined with diffuse correlation tomography (DCT) for assessing new treatments under development. Previously, we have built prediction models using DCT-derived blood flow index to assess mouse bone graft and fracture healings [40,41]. Different from THC, blood flow is another critical parameter which indicates the perfusion of major blood contents such as red blood cells. The THC from the SFDI and the blood flow index from DCT can be combined to build an improved multi-parametric prediction model to estimate the healing outcomes. By doing so, the healing outcome of the treatment and control groups can be assessed earlier than traditional methods. This will greatly expedite the development of new treatments.

5. Conclusion

In conclusion, we developed an SFDI technique dedicated to the mouse bone injury measurement. The longitudinal THC from our SFDI measurement agrees with the overall temporal expectation of vascularization in bone injury healing. The higher relative THC observed in the autograft group than in the allograft group was verified by the LME model, and the result matches the physiological expectation.

Funding

Acknowledgements

We thank Prof. Darren Roblyer at Boston University and OpenSFDI.org for their valuable advices and suggestions in building the SFDI instrument.

Disclosures

The authors declare no conflicts of interest.

References

1. A. S. Greenwald, S. D. Boden, V. M. Goldberg, Y. Khan, C. T. Laurencin, and R. N. Rosier, "Bone-graft substitutes: facts, fictions, and applications," J. Bone Jt. Surg., Am. Vol. **83**, 98–103 (2001).
2. P. V. Giannoudis, H. Dinopoulos, and E. Tsiridis, "Bone substitutes: an update," Injury **36**(3), S20–S27 (2005).
3. I. Pountos and P. V. Giannoudis, "Is there a role of coral bone substitutes in bone repair?" Injury **47**(12), 2606–2613 (2016).
4. H. J. Mankin, F. J. Hornicek, and K. A. Raskin, "Infection in massive bone allografts," Clin. Orthop. Relat. Res. **432**, 210–216 (2005).
5. D. L. Wheeler and W. F. Enneking, "Allograft bone decreases in strength in vivo over time," Clin. Orthop. Relat. Res. **435**, 36–42 (2005).
6. M. D. Hoffman, C. Xie, X. Zhang, and D. S. W. Benoit, "The effect of mesenchymal stem cells delivered via hydrogel-based tissue engineered periosteum on bone allograft healing," Biomaterials **34**(35), 8887–8898 (2013).
7. M. D. Hoffman and D. S. Benoit, "Emulating native periosteum cell population and subsequent paracrine factor production to promote tissue engineered periosteum-mediated allograft healing," Biomaterials **52**, 426–440 (2015).
8. X. Zhang, C. Xie, A. S. Lin, H. Ito, H. Awad, J. R. Lieberman, P. T. Rubery, E. M. Schwarz, R. J. O'Keefe, and R. E. Guldberg, "Periosteal progenitor cell fate in segmental cortical bone graft transplantations: implications for functional tissue engineering," J. Bone Miner. Res. **20**(12), 2124–2137 (2005).
9. C. Xie, D. Reynolds, H. Awad, P. T. Rubery, G. Pelled, D. Gazit, R. E. Guldberg, E. M. Schwarz, R. J. O'Keefe, and X. P. Zhang, "Structural bone allograft combined with genetically engineered mesenchymal stem cells as a novel platform for bone tissue engineering," Tissue Eng. **13**(3), 435–445 (2007).
10. H. Ito, M. Koefoed, P. Tiyapatanaputi, K. Gromov, J. J. Goater, J. Carmouche, X. Zhang, P. T. Rubery, J. Rabinowitz, R. J. Samulski, T. Nakamura, K. Soballe, R. J. O'Keefe, B. F. Boyce, and E. M. Schwarz, "Remodeling of cortical bone allografts mediated by adherent rAAV-RANKL and VEGF gene therapy," Nat. Med. **11**(3), 291–297 (2005).
11. R. S. Dhillon, C. Xie, W. Tyler, L. M. Calvi, H. A. Awad, M. J. Zuscik, R. J. O'Keefe, and E. M. Schwarz, "PTH-Enhanced Structural Allograft Healing Is Associated With Decreased Angiopoietin-2–Mediated Arteriogenesis, Mast Cell Accumulation, and Fibrosis," J. Bone Miner. Res. **28**(3), 586–597 (2013).
12. L. C. Gerstenfeld, D. M. Cullinane, G. L. Barnes, D. T. Graves, and T. A. Einhorn, "Fracture healing as a post-natal developmental process: Molecular, spatial, and temporal aspects of its regulation," J. Cell. Biochem. **88**(5), 873–884 (2003).
13. T. A. Einhorn and L. C. Gerstenfeld, "Fracture healing: mechanisms and interventions," Nat. Rev. Rheumatol. **11**(1), 45–54 (2015).
14. J. A. Buza and T. Einhorn, "Bone healing in 2016," Clin. Cases. Miner. Bone. Metab. **13**(2), 101–105 (2016).
15. R. E. Tomlinson and M. J. Silva, "Skeletal Blood Flow in Bone Repair and Maintenance," Bone Res. **1**(4), 311–322 (2013).
16. T. T. Roberts and A. J. Rosenbaum, "Bone grafts, bone substitutes and orthobiologics: The bridge between basic science and clinical advancements in fracture healing," Organogenesis **8**(4), 114–124 (2012).
17. J. K. Hoffman, S. Geraghty, and N. M. Protzman, "Articular cartilage repair using marrow stimulation augmented with a viable chondral allograft: 9-month postoperative histological evaluation," Case Rep. Orthop. **2015**, 617365 (2015).
18. D. G. Reynolds, C. Hock, S. Shaikh, J. Jacobson, X. Zhang, P. T. Rubery, C. A. Beck, R. J. O'Keefe, A. L. Lerner, E. M. Schwarz, and H. A. Awad, "Micro-computed tomography prediction of biomechanical strength in murine structural bone grafts," J. Biomech. **40**(14), 3178–3186 (2007).
19. E. A. Fragogeorgi, M. Rouchota, M. Georgiou, M. Velez, P. Bouziotis, and G. Loudos, "In vivo imaging techniques for bone tissue engineering," J. Tissue Eng. **10**, 204173141985458 (2019).
20. L. V. Wang and J. Yao, "A practical guide to photoacoustic tomography in the life sciences," Nat. Methods **13**(8), 627–638 (2016).
21. N. M. Tole, "Basic physics of ultrasonographic imaging," (2005).
22. D. J. Cuccia, F. Bevilacqua, A. J. Durkin, and B. J. Tromberg, "Modulated imaging: quantitative analysis and tomography of turbid media in the spatial-frequency domain," Opt. Lett. **30**(11), 1354–1356 (2005).
23. D. J. Cuccia, F. Bevilacqua, A. J. Durkin, F. R. Ayers, and B. J. Tromberg, "Quantitation and mapping of tissue optical properties using modulated imaging," J. Biomed. Opt. **14**(2), 024012 (2009).
24. J. P. Angelo, S.-J. Chen, M. Ochoa, U. Sunar, S. Gioux, and X. Intes, "Review of structured light in diffuse optical imaging," J. Biomed. Opt. **24**(07), 1 (2018).

25. S. Tabassum, Y. Zhao, R. Istfan, J. Wu, D. J. Waxman, and D. Roblyer, "Feasibility of spatial frequency domain imaging (SFDI) for optically characterizing a preclinical oncology model," Biomed. Opt. Express **7**(10), 4154 (2016).

26. A. Ponticorvo, D. M. Burmeister, R. Rowland, M. Baldado, G. T. Kennedy, R. Saager, N. Bernal, B. Choi, and A. J. Durkin, "Quantitative long-term measurements of burns in a rat model using Spatial Frequency Domain Imaging (SFDI) and Laser Speckle Imaging (LSI)," Lasers Surg. Med. **49**(3), 293–304 (2017).

27. A. J. Lin, G. Liu, N. A. Castello, J. J. Yeh, R. Rahimian, G. Lee, V. Tsay, A. J. Durkin, B. Choi, F. M. LaFerla, Z. Chen, K. N. Green, and B. J. Tromberg, "Optical imaging in an Alzheimer's mouse model reveals amyloid-β-dependent vascular impairment," Neurophoton **1**(1), 011005 (2014).

28. A. M. Laughney, V. Krishnaswamy, E. J. Rizzo, M. C. Schwab, R. J. B. Jr, D. J. Cuccia, B. J. Tromberg, K. D. Paulsen, B. W. Pogue, and W. A. Wells, "Spectral discrimination of breast pathologies in situusing spatial frequency domain imaging," Breast Cancer Res. **15**(4), R61 (2013).

29. J. B. Travers, C. Poon, D. J. Rohrbach, N. M. Weir, E. Cates, F. Hager, and U. Sunar, "Noninvasive mesoscopic imaging of actinic skin damage using spatial frequency domain imaging," Biomed. Opt. Express **8**(6), 3045–3052 (2017).

30. M. D. Reisman, Z. E. Markow, A. Q. Bauer, and J. P. Culver, "Structured illumination diffuse optical tomography for noninvasive functional neuroimaging in mice," Neurophotonics **4**(2), 021102 (2017).

31. S. Nandy, A. Mostafa, P. D. Kumavor, M. Sanders, M. Brewer, and Q. Zhu, "Characterizing optical properties and spatial heterogeneity of human ovarian tissue using spatial frequency domain imaging," J. Biomed. Opt. **21**(10), 101402 (2016).

32. "SAS Institute Inc., SAS OnlineDoc, Version 8, Cary, NC: SAS Institute Inc.," (1999).

33. A. Schindeler, M. M. McDonald, P. Bokko, and D. G. Little, "Bone remodeling during fracture repair: The cellular picture," Semin. Cell Dev. Biol. **19**(5), 459–466 (2008).

34. A. Ozaki, M. Tsunoda, S. Kinoshita, and R. Saura, "Role of fracture hematoma and periosteum during fracture healing in rats: interaction of fracture hematoma and the periosteum in the initial step of the healing process," J. Orthop. Sci. **5**(1), 64–70 (2000).

35. C. Lu, N. Saless, X. Wang, A. Sinha, S. Decker, G. Kazakia, H. Hou, B. Williams, H. M. Swartz, T. K. Hunt, T. Miclau, and R. S. Marcucio, "The role of oxygen during fracture healing," Bone **52**(1), 220–229 (2013).

36. K. Schilling, M. El Khatib, S. Plunkett, J. Xue, Y. Xia, S. A. Vinogradov, E. Brown, and X. Zhang, "Electrospun Fiber Mesh for High-Resolution Measurements of Oxygen Tension in Cranial Bone Defect Repair," ACS Appl. Mater. Interfaces **11**(37), 33548–33558 (2019).

37. C. K. Hayakawa, K. Karrobi, V. Pera, D. Roblyer, and V. Venugopalan, "Optical sampling depth in the spatial frequency domain," J. Biomed. Opt. **24**(07), 1–14 (2018).

38. S. L. Jacques, "Corrigendum: Optical properties of biological tissues: a review," Phys. Med. Biol. **58**(14), 5007–5008 (2013).

39. Y. Zhao, S. Tabassum, S. Piracha, M. S. Nandhu, M. Viapiano, and D. Roblyer, "Angle correction for small animal tumor imaging with spatial frequency domain imaging (SFDI)," Biomed. Opt. Express **7**(6), 2373–2384 (2016).

40. S. Han, A. R. Proctor, J. Ren, D. S. W. Benoit, and R. Choe, "Temporal blood flow changes measured by diffuse correlation tomography predict murine femoral graft healing," PLoS One **13**(5), e0197031 (2018).

41. J. Ren, S. Han, A. R. Proctor, D. E. Desa, G. A. Ramirez, V. R. D. Ching-Roa, J. B. Majeski, I. A. Dar, N. E. Barber, A. M. Forti, D. S. W. Benoit, and R. Choe, "Longitudinal 3D Blood Flow Distribution Provided by Diffuse Correlation Tomography during Bone Healing in a Murine Fracture Model," Photochem. Photobiol. **96**(2), 380–387 (2020).